Using thermal airborne imagery to measure near surface hydrology in upland ecosystems

Journal:	*Hydrological Processes*
Manuscript ID:	HYP-14-0162.R1
Wiley - Manuscript type:	Research Article
Date Submitted by the Author:	02-Jul-2014
Complete List of Authors:	Luscombe, David; University of Exeter, Geography, College of Life and Environmental Sciences Anderson, Karen; University of Exeter, Environment and Sustainability Institute Gatis, Naomi; University of Exeter, Geography, College of Life and Environmental Sciences Grand-Clement, Emilie; University of Exeter, Geography, College of Life and Environmental Sciences Brazier, Richard; University of Exeter, Life and Environmental Sciences
Keywords:	LiDAR, thermal imagery, peatland, ecohydrology

Using thermal airborne imagery to measure near surface hydrology in upland ecosystems

David J. Luscombe[1], Karen Anderson[2], Naomi Gatis[1], Emilie Grand-Clement[1] and Richard E. Brazier[1]

[1] Geography, CLES, University of Exeter, Amory Building, Rennes Drive, Exeter, Devon EX4 4RG

[2] Environment and Sustainability Institute, University of Exeter, Cornwall Campus, Treliever Road, Penryn, Cornwall, TR10 9EZ

1 Abstract

Upland ecosystems are recognized for their importance in providing valuable ecosystem services including; water storage, water supply and flood attenuation alongside carbon storage and biodiversity. The UK contains 10-15% of the global resource of upland blanket peatlands the hydrology and ecology of which is highly sensitive to external anthropogenic and climatic forcing. In particular, drainage of these landscapes for agricultural intensification and peat extraction has resulted in often unquantified damage to the peatland hydrology, and little is understood about the spatially distributed impacts of these practices on near surface wetness. This paper develops new techniques to extract spatial data describing the near surface wetness and hydrological behaviour of drained blanket peatlands using airborne thermal imagery and airborne LiDAR data. The relative thermal emissivity (ε_r) of the ground surface is mapped and used as a proxy for near surface wetness. The results show how moorland drainage and land surface structure have an impact on airborne measurements of thermal emissivity. Specifically, we show that information on land surface structure derived from LiDAR can help normalise signals in thermal emissivity data to improve description of hydrological condition across a test catchment in Exmoor, UK. An *in situ* field hydrological survey was used to validate these findings. We discuss how such data could be used to describe the spatially distributed nature of near surface water resources, to optimize catchment management schemes and to deliver improved understanding of the drivers of hydrological change in analogous ecosystems.

Keywords: LiDAR, thermal imagery, peatland, ecohydrology.

2 Introduction

Globally, peat covered landscapes are recognized for their importance in providing valuable ecosystem services such as water and carbon storage, water supply and flood attenuation (Cannell *et al.*, 1993; Joosten and Clarke, 2002; Bellamy *et al.*, 2005). The UK contains 10-15% of the global resource of upland blanket peatlands (Tallis, 1998; Wilson *et al.*, 2010), the formation, functioning and persistence of which is principally controlled by the availability of water and its loss from the system. Downstream these peatlands also provide significant hydrological inputs to the public water supply system (Worrall *et al.*, 2007) and are located at the headwaters of some of the UK's most "flashy" and therefore flood prone river systems (Holden *et al.*, 2006). However, the hydrology and ecology of peatlands is highly sensitive to anthropogenic disturbance and climatic forcing (Charman, 2002; Reed *et al.*, 2009). Surface wetness, water table depth, flow pathways and rainfall-runoff dynamics are known to be dramatically modified in damaged and drained peatland landscapes (Holden *et al.*, 2004; Holden *et al.*, 2006; Wilson *et al.*, 2010). Consequently, understanding the spatial heterogeneity of the water resource and topography in these landscapes is critical in effectively managing the peatland resource and its ecosystem services. Accordingly, there is a growing need for accurate, spatially distributed information describing the hydrological condition of these upland ecosystems (Harris and Bryant, 2009). Such information could be used to optimize and focus catchment management schemes and allow for enhanced understanding of the drivers of hydrological change (Grand-Clement *et al.*, 2013).

Currently, baseline and post-restoration monitoring of hydrological parameters in peatlands is limited and in many cases data are not fully spatially interrogated or structured (Wilson *et al.*, 2010). The widespread availability of fine-scale remote sensing technologies for quantifying landscape structure and function presents an opportunity to improve understanding of the hydrological functioning of these systems over landscape extents (Gert *et al.*, 2011). Already, there is evidence that airborne Light Detection and Ranging (LiDAR) data can provide useful data for monitoring habitat vegetation structure and landscape morphology as proxies for hydrological condition (Clawges *et al.*, 2008; Vierling *et al.*, 2008; Horning *et al.*, 2010; Chassereau *et al.*, 2011). In peatlands, these data have been used to describe vegetation and surface structure in order to improve interpretation of eco-hydrological function (Anderson *et al.*, 2009; Anderson *et al.*, 2010; Luscombe *et al.,* 2014). LiDAR technology is also becoming increasingly widely used by scientists at the landscape scale to describe the complexities of wetland and fluvial ecosystems and to develop numerical models which

quantify the hydrological functioning of these systems (James *et al.*, 2007; Vierling *et al.*, 2008; Korpela *et al.*, 2009; Anderson *et al.*, 2010; Bertoldi *et al.*, 2011; Hutton and Brazier, 2012). For example, studies exist that show the use of LiDAR DEMs for deriving flow accumulation, rainfall runoff estimates and indices of spatial near surface wetness (Lamb *et al.*, 1998; Beven and Freer, 2001). All such numerical models are inherently uncertain, (Beven, 2012) and independent spatially distributed information (rather than, or in addition to discrete *in situ* observations) describing hydrological parameters or conditions would help towards validating the complex story of water storage and loss in these systems.

There is an opportunity in using multi-sensor approaches to address this challenge, by combining LiDAR with other remote sensing tools that can more directly describe spatial variability in indicators of near-surface wetness. A relatively under-explored option in this domain is the use of airborne thermal imagery (sometimes called 'thermography'), which can characterise spatial patterns in landscape relative thermal emissivity (ε_r). Such data can in theory, indicate patterns of land near surface wetness (Price, 1980) because ε_r is reliant upon the relatively high specific heat capacity (C) of water (4.1855 J/g-K^{-1} at 15°C, 101.325 kPa) and its ability to resist heat loss being higher than surrounding landscape components. In cool air temperatures water masses can consequently appear warm relative to their surroundings, and in a landscape context this could facilitate detection of the relative moisture content of the soil (Price, 1980; Campbell, 1996). There are some complexities – for example, ε_r provides only a relative thermal measurement that will vary according to the thermodynamic properties of the surface (i.e. wet vs. dry masses) and/or the ability of a material or structure to retain or emit energy (Anderson and Wilson, 1984; Campbell, 1996). Therefore, more highly structured vegetation (e.g. trees) will have higher relative measurements of ε_r. Similarly, changes in topography can affect the mixing of air masses and the measured ε_r due to the relative position of the sensor (Torgersen *et al.*, 2001). Such effects cause equifinality in the interpretation of these data in heterogeneous landscapes and have previously limited the use of thermal airborne imaging (Quattrochi and Luvall, 1999).

Using LiDAR and airborne thermal imagery together, we propose that vegetation composition and structure may be "disentangled" from other features and used to understand the nature of underlying surface wetness and the associated eco-hydrological processes. Furthermore, models of surface flow pathways and wetness indices generated from LiDAR Digital Surface Model's (DSM's) may then be integrated alongside the extent of near surface

wetness available from airborne thermal imaging data, to improve the understanding of near surface water flow pathways in peatlands.

2.1 Aims and Hypotheses

This paper develops new techniques aimed at understanding the near-surface hydrological information contained within fine scale thermal remote sensing data of an upland peatland catchment. The study utilised data from the Itres Instruments Thermal Airborne Broadband Imager (TABI) coupled with simultaneously collected data from an airborne LiDAR sensor (ALTM Gemini (08SEN230) LIDAR instrument). The data presented explore how TABI data can be used to understand, and potentially quantify, near surface wetness in such wetlands.

This paper tests the following hypotheses:

1. Patterning evident in unprocessed ε_r data from airborne TABI thermographs is spatially associated with the position of anthropogenic drainage networks.

2. Structural data from LiDAR datasets covering the same extent as ε_r data distinguishes areas where structure or wetness dominates emissivity measurements.

3. Structurally normalized TABI ε_r data are related to the spatial distribution of near surface wetness in an upland peatland.

3 Methods

3.1 Study Area and Data collection.

Our approach employed airborne LiDAR and TABI data captured and processed by the UK Environment Agency Geomatics Group in May 2009. The Itres Instruments Thermal Airborne Broadband Imager (TABI) provided thermal imagery at 2 m × 2 m spatial resolution and better than 0.1 ^{o}C noise equivalent temperature difference (NEDT). LiDAR data were collected using an ALTM Gemini (08SEN230) LIDAR instrument and were supplied as a pre-derived but unfiltered DSM dataset, with a 0.5 m × 0.5 m spatial resolution. The LiDAR dataset was checked for accuracy at five separate locations by the Geomatics group, using a differential Global Positioning System (DGPS) survey. These ground truth data indicated an average systematic error of + 0.0004 m and an average random bias of ± 0.047 m in elevation. The combined root-mean-square error (RMSE) for these data was 0.029 m which was within the product specification of 0.15 m (pers. Comm. 2012).

The ε_r data from TABI describe the thermal energy emission of an observed mass or structure (Avery and Berlin, 1992). However, as ε_r data are not fully calibrated to land surface temperature or material emissivity (the ratio of thermal emission to that of a black body of the same temperature), the data obtained only provide relative values. Furthermore, the resultant ε_r data contain measurements describing the temperature of the observed surface combined with the effect of the material emissivity of the target. The TABI and LiDAR data were collected at a single flying height (800 – 1000 m above ground level) and due to the different radiometric properties of the two sensors, this gave rise to datasets with different spatial resolutions.

Data were extracted for a highly instrumented experimental headwater catchment in Exmoor National Park named “Spooners” (51° 7'26.77"N, 3°44'55.96"W, elevation range 376 to 443m asl). The catchment was selected to include a representative range of drainage ditch morphology, slope morphology, aspect and vegetation composition typical of the area and to exclude land use types not representative of the wider peatland landscape in Exmoor National Park. The location of the watershed of the study catchment is shown in Figure 1 alongside visualizations of the visible and LiDAR data available for that watershed.

3.2 Initial exploration of patterns in the data

To understand the broad-scale landscape patterning evident in the TABI dataset a preliminary exploration of the data was undertaken. Spatial patterns in ε_r over the catchment were examined by first, overlaying the TABI dataset on a LiDAR elevation model, and then assigning colours to the measured ε_r values and stretching the colour ramp to increase visual differentiation of ε_r. The thematic analysis of this data sought to inform later stages of the data processing.

3.3 Association of TABI with surface drainage

The locations of anthropogenic drainage channels within the Spooners catchment were initially identified using fine scale aerial photography. Subsequently in 2011, the channel positions were mapped and verified during detailed site walkovers. A hand held GPS unit with a spatial accuracy of < 1m (Thales Navigation, MobileMapper CE) was used to record the position of these features. Once identified each drain was measured by walking the length of the feature and new line segments were recorded where any step change in the morphology or vegetation on the surface drain was evident. Each line segment therefore had metadata describing the approximate height, width, cross sectional profile and dominant vegetation recorded. These linear vector features were subsequently exported from the GPS and overlaid onto the TABI ε_r dataset within ArcGIS. This allowed hypothesis one to be evaluated as it was then possible to understand the spatial relationship between the locations of drainage features and the patterns evident in the TABI ε_r dataset.

3.4 Normalizing TABI data using structure.

3.4.1 Exploring spatial and vertical structures in vegetation across the catchment

The first stage in understanding how best to correct the TABI ε_r data for structural variability was to assess the nature of changes in the surface structure across the catchment. Firstly, data subsets were generated for nine areas of interest (AOI) measuring approximately 20 m × 20 m. These were three manually selected areas of high (>0.64), intermediate (-1.51 to -2.6) and low (<-2.60) ε_r pixel values identified in the raw TABI ε_r data (classified using the Jenks natural breaks method) that were large enough to accommodate the AOI neighbourhood. The location of these is shown in Figure 2.

Using the LiDAR data, each AOI was analysed geostatistically to quantify the scale of surface patterns in the detrended LiDAR DSM. In each case, LiDAR data were first

numerically filtered using a "low pass" moving window across the data using an 11 × 11 pixel neighbourhood, resulting in a "smoothed" surface. These data were then subtracted from the original dataset to derive a "detrended" dataset showing only the high frequency spatial variation. Secondly, the geostatistical approach employed semivariogram analysis in which dissimilarity (γ) of pairs of points (N) are described as a function of separation distance (h) across the surface, as in the empirical variogram in Eq. 1. This technique describes the spatial dependence of values in the LiDAR DSM AOI data subsets (Anderson *et al.*, 2009).

$$\hat{\gamma}(\boldsymbol{h}) := \frac{\mathbf{1}}{|\boldsymbol{N}(\boldsymbol{h})|} \sum_{(\boldsymbol{i},\boldsymbol{j})\epsilon\boldsymbol{N}(\boldsymbol{h})} \left|\boldsymbol{z_i} - \boldsymbol{z_j}\right|^{\mathbf{2}} \qquad (\mathbf{1})$$

An ordinary spherical model was fitted to the resultant data for each AOI as this was found to best fit the empirical semivariograms generated. Alongside the model, three key parameters derived from this analysis are the sill variance, which describes the total variability (of height (z) values) in the data, the nugget which describes error and variability below the sampling interval (pixel size) and the range. Importantly, the range describes the distance at which values cease to show spatial autocorrelation and therefore is indicative of the length scale of the measured surface structure. These parameters were extracted for each of the AOI's for comparison. A descriptive classification of the dominant vegetation community was also created for each AOI from super-high resolution (0.2 x 0.2m cell size) aerial photography collected in March 2012 and confirmed with field surveying. Vegetation was classified broadly into areas dominated by Juncus spp. (soft rush), Molinia caerulea (purple moor grass), wet bog communities, and minerotrophic grassland communities. Molinia dominated areas were also classified as having "wet" or "dry" ground surfaces as this species can physiologically adapt to wetness and persist in both situations. These data were used to inform the optimal method for generating surface roughness estimates from LiDAR.

3.4.2 Generating a structural index of surface roughness from LiDAR

As ε_r are known to be in part affected by the structural attributes of an observed surface (Campbell, 1996), it was necessary to take steps towards normalising the TABI ε_r dataset for surface roughness changes. An index of surface roughness could be easily calculated for each LiDAR pixel. This was achieved using the method described fully in Jenness (2004), whereby the triangular surface area of each pixel is calculated, and then divided by the respective planar surface area. The result is a ratio between the planar and angular surface area which is indicative of a surface roughness index (SRI). This method, combined with the

fine resolution DSM used, results in a more accurate measure of 3D topographic roughness in the LiDAR than detrending the data and deriving a neighbourhood standard deviation index of roughness (Cavalli *et al*., 2008). This is because the values in the wider neighbourhood of the pixel do not influence the calculation result (Jenness, 2004). The derived data were deemed most appropriate to test the full structural associations (i.e. *x,y* and *z* variation) with measured ε_r values in the TABI dataset. These data were also processed in Esri ARCGIS v. 9.3.1, to aggregate pixel values from the 0.5m LiDAR data to a 2 m resolution, so as to match the spatial resolution of the TABI dataset with which it was compared. Prior to full normalization using these data, it was necessary to rescale the SRI data layer and the TABI ε_r layer to between 0 and 1, to ensure representative control on the output values. The result of this processing was a re-scaled 2m SRI dataset that could be used to normalize the re-scaled TABI ε_r data.

3.4.3 Normalising TABI according to a LiDAR-derived surface roughness index

The resultant data were used to create a normalised TABI dataset of the same extent and spatial resolution by calculating a simple ratio of emissivity to "roughness", i.e. TABI ε_r divided by SRI index value. The result was a 2m normalized TABI ε_r dataset that could be used to assess non-structurally related changes in ε_r across the catchment in relation to field validation data. Derived data were also non dimensional (i.e. unitless), however as TABI data are only examined as relative measurements in this study; this did not affect further analysis.

3.5 Validation of normalized TABI

In order to validate the hypothesized spatial distribution of surface wetness evident in the TABI data (hypothesis 3), field measurements of surface wetness were required as an independent test dataset. Data were collected at 100 randomly located points within the catchment that were pre-determined according to a random point generator in ArcGIS version 10. Each of the point locations within the catchment were identified using the same handheld GPS as previously described and visited in December 2013. The presence or absence of the water table from the surface to a depth of >10 cm was recorded at each point, against a nominal four class scale (Table 1). A 0.1 m × 0.1 m × 0.2 m test pit was used to measure depth of water table where it was not visible at the surface. This classification system was used because instrumentation (theta probe) trialled at the catchment in 2012 to record soil surface moisture content failed to differentiate water content within any of the peat soils examined, and all readings were returned as showing full saturation. The four point scale was

also straightforward to capture, across a large number of points and allowed differentiation between observed surface wetness characteristics throughout the catchment. The locations and values of these 100 points were imported into ArcGIS and overlaid on the normalized TABI dataset developed in the previous stage. To aid the visual comparison of these data with $\mathcal{E}_{r,}$ the points were then interpolated using a simple Natural Neighbour (NN) algorithm in ArcGIS 10. The result was an interpolated map of estimated *in situ* surface wetness that could be used as an independent comparison with the information content of the roughness normalized TABI $\mathcal{E}_r$ data. The interpolated data allow for a simple visual comparison of the spatial patterning of these data across the catchment extent. However, as the interpolated dataset uses nominal integer values as an input, further quantitative interrogation of these data would include error propagated via the NN interpolation. As such, quantitative analysis was based on the 100 point measured dataset.

4 Results

4.1 Initial exploration of patterns in the data

Figure 3 shows an overlay of the raw TABI dataset over a basic topographic hill shade model from the LiDAR data. Areas of higher emissivity (red) appear to be concentrated in topographic sinks and also form linear and connected features across the wider catchment indicative of the surface flow networks found in upland peatland landscapes. Areas of higher ε_r also appear coincidental with large structural features such as the square tree bordered enclosure and the boundary fence lines. These findings supported further examination of the relationship between TABI data and models of land surface structure derived from LiDAR data.

4.2 Association of TABI with surface drainage (Hypothesis 1)

A simple comparison between raw TABI ε_r and drainage networks (figure 4) illustrates that in those areas where anthropogenic drainage networks are intact and functional, ε_r is generally lower. Rapid transitions between higher and lower ε_r also appear to be coincidental with the direction and location of drainage features (arrow 3, Figure 4). Assuming that those areas where drainage features are present are less likely to hold significant surface water, this finding suggests the areas with higher ε_r may be wetter. However, areas of high surface structure variability (hitherto referred to as roughness) such as trees (arrow 2, figure 4) appear to have a very strong control on the recorded ε_r value. Some transitions in ε_r also appear to be independent of any drainage features (arrow 1, figure 4).

4.3 Normalizing TABI data using structure (Hypothesis 2)

4.3.1 Exploring spatial and vertical structures in vegetation across the catchment.

The geostatistical interrogation of the detrended LiDAR data in each AOI provides further information on the relationship between roughness and ε_r. The semivariogram models plotted for each AOI in figure 2 (key statistics extracted in Table 2) demonstrate significant variation relating to the vertical scale and variability of the structures present in each area.

Firstly, Figure 5 shows that for the three AOI types shown in Figure 2 (with high (red), intermediate (yellow) and low (blue) thermal emissivity), the semivariogram range values (table 2) show little variation. Range values are indicative of the length scale (patch size) of

surface features within each AOI and only vary between 1.38m to 2.43m across all of the AOIs studied. This indicates that the patch size of the vegetation exhibits low spatial variation across the catchment, and corroborates results from other studies that show similar length scales in peatland vegetation pattern (Anderson *et al.*, 2009). This finding shows that the horizontal scale of the vegetation patterning across these AOIs is quite consistent regardless of ε_r.

In contrast, Figure 5 shows that the total variability in DSM height is much more variable from site to site, as indicated by changes in sill variance across these AOIs. AOIs with higher ε_r are shown to have the highest sill variances (and thus the highest total spatial variation in LiDAR DSM height), whilst areas of low ε_r have the lowest sill variances (and thus lower total spatial variation in LiDAR height). Areas of intermediate ε_r are seen to have a spread of sill variance values. This relationship may suggest that the areas with higher ε_r which may be wetter, exhibit taller and more variable vegetation or microtopographic structure. For example, dense *Juncus effusus* rush stands or separated *Molinia* tussocks where the vegetation/surface structure is more spatially separated allowing water to flow between plants. Indeed, the vegetation classes associated with these AOIs support this assumption with all three of the AOIs with the highest ε_r values having characteristic "wet" vegetation communities (table 2). Given this finding, and the assumption that roughness may directly affect ε_r values, it was necessary to take steps to normalise the effect of this structure on recorded ε_r.

4.3.2 Generating a structural index of surface roughness from LiDAR

The index of roughness (SRI) generated according to the method explained in 3.4.2 resulted in a raster dataset with distinct patternation illustrating a square tree bordered enclosure, multiple anthropogenic drainage ditches and patternation indicative of shifts in ecological structure (figure 6) across the catchment. Once aggregated to a pixel size equivalent to that of the TABI dataset (2 m), these data were able to be used to derive fine scale normalisation of the TABI data using this structural proxy.

4.3.3 Normalising TABI according to a LiDAR-derived surface roughness index

The normalisation of the TABI data generated a dataset describing ε_r without the direct influence of surface/vegetation structure. Figure 7 illustrates that the square tree bordered enclosure and key areas of the channel network (with incised fluvial topography) are

"corrected" so that they now show reduced relative ε_r values. This result suggested that the method was successful in mitigating the effect of structure on ε_r.

4.4 Validation of normalized TABI (Hypothesis 3)

4.4.1 Field survey of surface moisture variations

Data displayed in figure 7 illustrate a clear spatial relationship between those areas with a higher mapped wetness value and higher normalised ε_r, with both hypothesised areas of surface wetness and known drainage features corresponding well. Assuming that ε_r is describing wetness to some level, this relationship suggests that patterns of ε_r in this catchment are describing patterns of wetness related to important hydrological processes. It is important to note that there was a time lag between the remote sensing survey and the ground wetness survey, but hydrological conditions were not known to have changed between these dates, so the comparison should be robust.

4.4.2 Interpolated model of field-validated surface moisture variation

Interpolation of these field wetness measurements using a NN algorithm produced a clear visualisation of results previously shown in Figure 7. These data (Figure 8) also support the spatial association between surface wetness and ε_r across the entire catchment. However, as this interpolation technique is numerically simple and unconstrained by surface channels or drainage features, some areas of wetness appear to be overrepresented in the resultant dataset.

4.4.3 Intercomparison of TABI-E and field model

The spatial association between the normalised TABI values and recorded surface wetness are illustrated in figure 9 as a boxplot of the normalised ε_r recorded at each of the field survey points (n=100), split into each of the four wetness classes (table 1). These data illustrate that ε_r increases with increasing surface wetness and that the areas with the highest measured surface wetness demonstrate a consistently higher ε_r value. Variation evident in these data is likely to be due to the compound effect of several factors:

1. Unconstrained interpolation of wetness associated with constrained wetness pathways, i.e. drainage channels and ditches.
2. Temporal separation in the sampling of the datasets.
3. Microclimatic variation due to the topographic/structural constraint of air masses.

4. The direct effect of using integer scores in assessing ε_r. I.e. as wetness values at each location are discrete, the modelled or actual values of surface wetness are always subject to an implicit uncertainty.

Simple statistical analysis of the variance in ε_r within each wetness class, (Kruskal- Wallis test) suggests that the overall, emissivity values vary significantly ($p < 0.001$) between the wetness classes. Further post-hoc analysis of these data (Mann-Whitney u-test) suggests that, alternate groups (i.e. 1-3 and 2-4) are statistically different from one another ($p<0.05$), and that the direct difference between groups 3 and 4 is also significant ($p<0.05$). These data, therefore, are strongly suggestive of wetness directly controlling the measured ε_r.

5 Discussion

A spatial understanding of how the water is distributed in peatland landscapes is key to understanding ecosystem services and modelling hydrological functioning of peatland catchments (Harris and Bryant, 2009). For a peatland landscape which may be dominated by saturation excess overland flow (Charman, 2002; Grayson *et al.*, 2010) the spatial distribution of near surface wetness over large spatial extents provides important information in the understanding of hydrological and ecological condition (Goward *et al.*, 2002). Whilst numerous studies model the spatial distribution of surface wetness (Lamb *et al.*, 1998; Beven and Freer, 2001; Gallart *et al.*, 2007), there are few studies that show how near surface wetness can be measured across large spatial extents to support such work. In response to our three hypotheses we have found the following:

1. Patterning evident in unprocessed ε_r data from airborne TABI thermographs is spatially associated with the position of anthropogenic drainage networks.

Our initial analysis shown in figure 4 indicated a visual spatial association between areas of high and low emissivity from TABI, and the presence of anthropogenic drainage channels in the catchment. Given this positioning of the patterning in raw ε_r relative to channels in the peatland (figure 4), it is reasonable to conclude that these data could be used to describe relative near surface wetness across the catchment, and that this technique presents a new method to evaluate and map the distribution of near surface water in analogous catchment systems.

2. Structural data from LiDAR datasets covering the same extent as ε_r data distinguishes areas where structure or wetness dominates emissivity measurements.

One key aspect that needs to be borne in mind when using thermography for surface wetness mapping is that other landscape variables can also impact on the values of ε_r measured by a system such as TABI. In this work, surface structure is shown to be a major control on patterns of ε_r and needs to be corrected or normalised before the data can be used as a relative index of near surface wetness. Geostatistical analysis (Figure 5, Table 2) of the LiDAR dataset demonstrated that at a plot-scale, textural characteristics of the peatland surface relate to ε_r (i.e. the inferred relative wetness of that area), due to the effect of the local wetness on ecohydrological organization. However, the nature of the variation in these data (LiDAR) indicates that structural differences may be occurring as a response to wetness (observed in the thermal imaging) and not operating as a strong feedback on the measurement of ε_r. This relationship between wetness, structure and ε_r, supports the need to normalise the effect of ecosystem structure on measurements of ε_r, in order to better interpolate surface wetness.

Our approach utilised a fine scale LiDAR dataset that was able to describe changes in surface roughness across the catchment, in this case caused by different ecological communities in different hydrological zones. The resultant data demonstrate that in areas where raw ε_r measurements were higher due to more complex ecological or morphological structure, this approach was effective at normalising these data. The dataset derived therefore allows us to distinguish between areas of greater near-surface wetness and structural anomalies (i.e. trees, banks and fences) affecting ε_r (figure 6). However, there are areas of the resultant dataset that still appear to exhibit higher relative ε_r than may be expected. For example, the area surrounding (and within) the tree enclosure, exhibits high ε_r that may be indicative of regional microclimatic variations influencing the measured temperature and ε_r. Therefore, whilst this technique is useful for minimising the effects of surface roughness on ε_r, there are extraneous factors that must also be considered as potential causes of changes in ε_r and that are not moisture related.

3. Structurally normalized TABI ε_r data are related to the spatial distribution of near surface wetness in an upland peatland.

The results have shown that in using the LiDAR roughness to normalise ε_r values, it was possible to derive a dataset describing surface wetness well, when compared to in-situ field

measurements of near surface wetness (figure 8, figure 9). The analysis of *in situ* measurements of surface wetness and ε_r shows a statistically significant relationship between wetness measurements and TABI derived ε_r (figure 9). Furthermore, the spatial information in the structurally normalised TABI dataset exceeds that of the *in situ* wetness dataset, which are relatively coarse in comparison. Whilst structurally normalised TABI data are still subject to added uncertainty in ε_r from microclimatic and topographical drivers, these results suggest that these techniques will be useful in understanding surface wetness across similar landscapes. The coupled data approach presented here also provides useful cross evaluation of findings in both LiDAR and TABI datasets (Hyde *et al.*, 2006; Vierling *et al.*, 2008).

Unlike the deployment of such technologies from space-borne platforms (Quattrochi and Luvall, 1999), the ability of these airborne technologies in combination to characterize both the hydrological and ecological condition of these landscapes at a fine spatial scale, also makes them highly appropriate to be used as an ongoing management tool on annual or decadal scales. For instance, vegetation communities with characteristic architecture and with known tolerance to soil saturation could be differentiated (i.e. stands of *Juncuss spp* or areas dominated by *Sphagnum spp*) and their extents mapped. Similarly, regularly repeated surveys of these datasets could be used to quantify the fine scale shifts in ecohydrological structure in intact or degraded peatlands (Quattrochi and Luvall, 1999), such as the degradation of hummock-hollow micro topography in response to drier soils conditions (Korpela *et al.*, 2009). When data capture is repeated on a pre/post landscape restoration basis, this approach could offer potential as a tool for understanding the extent to which landscape alteration, such as artificial drainage, affects ecohydrological processes and pathways and the effectiveness of landscape restoration schemes in mitigating these affects and restoring ecosystem services. This technique could provide a quantitative measurement of the increase in surface wetness following restoration measures, such as the blocking of drains and ditches. Furthermore, this coupled technique allows us to measure the nature (i.e. diffuse or concentrated) and position of the surface flow pathways reinstated under such works, which is important in understanding the runoff dynamics in these modified systems. Repeating data collection with a high temporal frequency may also enable us to assess shifts in the storage of water in both surface pools and as near surface wetness across the upland landscapes.

Data used in this way can also be used to aid in the parameterization (or evaluation) of spatially distributed rainfall runoff models. Using distributed internal catchment

measurements to parameterize numerical models, has been shown to reduce uncertainty in numerical predictions of catchment behaviour (Lamb *et al.*, 1998; Gallart *et al.*, 2007). DSMs, such as those derived from LiDAR data, are key in developing numerical indices of hydrological behaviour used within rainfall runoff models such as TOPMODEL (Beven, 2012). Such indices form spatially integrated inputs to these models such as relative topographic wetness, relative local storage deficits, flow accumulation and contributing areas. Using TABI data in combination with DSM data to evaluate the spatial accuracy of these model predictions provides an opportunity to assess, modify and improve the spatial representation of the DSM derived inputs into such models and constrain model uncertainty and spatial equifinality (Brazier *et al.*, 2010). Using such data to improve the spatial quality of catchment models would improve the extent that landscape restoration effects can be predicted for many other analogous landscapes where comparable DSMs are available (Vierling *et al.*, 2008). Subsequently, those managing these landscapes and/or quantifying the impact of restoration works could be better able to predict effects across larger extents that are appropriate to the scale at which they need to plan restoration works and prove the efficacy of their interventions (Holden *et al.*, 2004).

6 *Conclusions*

In conclusion, this analysis demonstrates that patterning evident in the airborne thermal imagery is consistent with the positioning of anthropogenic drainage networks in this peatland. Airborne thermal imagery (TABI) and LiDAR data used in conjunction are also shown to aid interpretation of ε_r measurements and describe the extent of near surface wetness in many areas the studied landscape. Furthermore, this coupled approach proves to be useful in further interrogating the spatial patterning of vegetation types in response to wetness in upland landscapes. The datasets derived from this coupled approach also demonstrate potential for integration into other multi-scale approaches to understand analogous landscapes, including; numerical rainfall-runoff modelling, spatially distributed hydrological monitoring approaches and conventional plot based monitoring of vegetation communities. Critically, these data cover far larger extents and remote locations than field based monitoring would normally be able to achieve and can be used to cross-validate/supplement traditional monitoring of this type. Repeats of this analysis over different extents and utilizing thermal data of a higher resolution would further test this methodology and help develop datasets of near surface wetness useful to those managing

peatland landscapes. Importantly, repeated data capture following landscape restoration could enable the change in patterns of near surface wetness to be ascertained and therefore evaluate the effectiveness of restoration techniques on raising water tables at landscape scales.

7 *Reference List*

Anderson JM, Wilson SB. 1984. Review Article.The physical basis of current infrared remote-sensing techniques and the interpretation of data from aerial surveys. International Journal of Remote Sensing, **5**: 1-18. DOI: 10.1080/01431168408948786.

Anderson K, Bennie J, Wetherelt A. 2009. Laser scanning of fine scale pattern along a hydrological gradient in a peatland ecosystem. Landscape Ecology, **25**: 477-492. DOI: 10.1007/s10980-009-9408-y.

Anderson K, Bennie JJ, Milton EJ, Hughes PDM, Lindsay R, Meade R. 2010. Combining Lidar And Ikonos Data For Eco-hydrological Classification Of An Ombrotrophic Peatland. J. Environ. Qual., **39**: 260-273. DOI: 10.2134/jeq2009.0093.

Avery TE, Berlin TE. 1992. Fundamentals of remote sensing and airphoto interpretation. Macmillan.

Bellamy PH, Loveland PJ, Bradley RI, Lark RM, Kirk GJD. 2005. Carbon losses from all soils across England and Wales 1978-2003. Nature, **437**: 245-248.

Bertoldi W, Gurnell AM, Drake NA. 2011. The topographic signature of vegetation development along a braided river: Results of a combined analysis of airborne lidar, color air photographs, and ground measurements. Water Resour. Res., **47**: W06525. DOI: 10.1029/2010wr010319.

Beven K. 2012. Rainfall-Runoff Modelling, The Primer. Second Edn., John Wiley & Sons, Ltd.

Beven K, Freer J. 2001. A dynamic TOPMODEL. Hydrological Processes, **15**: 1993-2011. DOI: 10.1002/hyp.252.

Brazier RE, Hutton CJ, Parsons AJ, Wainwright J. 2010. In: Handbook of Erosion Modelling, Morgan RPC, Nearing MA (eds.) Blackwell,, pp: 98-117.

Campbell JB. 1996. Introduction to Remote Sensing. Second Edn., Taylor and Francis.

Cannell MGR, Dewar RC, PYATT DG. 1993. Conifer Plantations on Drained Peatlands in Britain: a Net Gain or Loss of Carbon? Forestry, **66**: 353-369. DOI: 10.1093/forestry/66.4.353.

Cavalli M, Tarolli P, Marchi L, Dalla Fontana G. 2008. The effectiveness of airborne LiDAR data in the recognition of channel-bed morphology. CATENA, **73**: 249-260.

Charman D. 2002. Peatlands and Environmental Change. John Wiley & Sons Ltd.

Chassereau JE, Bell JM, Torres R. 2011. A comparison of GPS and lidar salt marsh DEMs. Earth Surface Processes and Landforms, **36**: 1770-1775. DOI: 10.1002/esp.2199.

Clawges R, Vierling K, Vierling L, Rowell E. 2008. The use of airborne lidar to assess avian species diversity, density, and occurrence in a pine/aspen forest. Remote Sensing of Environment, **112**: 2064-2073.

Gallart F, Latron Jrm, Llorens P, Beven K. 2007. Using internal catchment information to reduce the uncertainty of discharge and baseflow predictions. Advances in Water Resources, **30**: 808-823. DOI: http://dx.doi.org/10.1016/j.advwatres.2006.06.005.

Goward SN, Xue Y, Czajkowski KP. 2002. Evaluating land surface moisture conditions from the remotely sensed temperature/vegetation index measurements: An exploration with the simplified simple biosphere model. Remote Sensing of Environment, **79**: 225-242.

Grand-Clement E, Anderson K, Smith D, Luscombe D, Gatis N, Ross M, Brazier RE. 2013. Evaluating ecosystem goods and services after restoration of marginal upland peatlands in South-West England. Journal of Applied Ecology, **50**: 324-334. DOI: 10.1111/1365-2664.12039.

Grayson R, Holden J, Rose R. 2010. Long-term change in storm hydrographs in response to peatland vegetation change. Journal of Hydrology, **389**: 336-343.

Harris A, Bryant RG. 2009. A multi-scale remote sensing approach for monitoring northern peatland hydrology: Present possibilities and future challenges. Journal of Environmental Management, **90**: 2178-2188.

Holden J, Chapman PJ, Labadz JC. 2004. Artificial drainage of peatlands: hydrological and hydrochemical process and wetland restoration. Progress in Physical Geography, **28**: 95–123.

Holden J, Evans MG, Burt TP, Horton M. 2006. Impact of Land Drainage on Peatland Hydrology. J. Environ. Qual., **35**: 1764-1778. DOI: 10.2134/jeq2005.0477.

Horning N, Robinson JA, Sterling EJ, Turner W, Spector S. 2010. Remote Sensing for Ecology and Conservation: A Handbook of Techniques., Oxford University Press.

Hutton C, Brazier RE. 2012. Quantifying riparian zone structure from airborne LiDAR: Vegetation filtering, anisotropic interpolation, and uncertainty propagation. Journal of Hydrology, **442-443**: 36-45.

Hyde P, Dubayah R, Walker W, Blair JB, Hofton M, Hunsaker C. 2006. Mapping forest structure for wildlife habitat analysis using multi-sensor (LiDAR, SAR/InSAR, ETM+, Quickbird) synergy. Remote Sensing of Environment, **102**: 63-73.

James LA, Watson DG, Hansen WF. 2007. Using LiDAR data to map gullies and headwater streams under forest canopy: South Carolina, USA. CATENA, **71**: 132-144.

Jenness JS. 2004. Calculating landscape surface area from digital elevation models. Wildlife Society Bulletin, **32**: 829-839. DOI: 10.2193/0091-7648(2004)032[0829:clsafd]2.0.co;2.

Joosten H, Clarke D. 2002. Wise Use of Mires and Peatlands. International Mire Conversation Group and International Peat Society.

Korpela I, Koskinen M, Vasander H, Holopainen M, Minkkinen K. 2009. Airborne small-footprint discrete-return LiDAR data in the assessment of boreal mire surface patterns, vegetation, and habitats. Forest Ecology and Management, **258**: 1549-1566.

Lamb R, Beven K, Myrab S. 1998. Use of spatially distributed water table observations to constrain uncertainty in a rainfall-runoff model. Advances in Water Resources, **22**: 305-317. DOI: http://dx.doi.org/10.1016/S0309-1708(98)00020-7.

Luscombe DJ, Anderson K, Gatis N, Wetherelt A, Grand-Clement E, Brazier RE. 2014. What does airborne LiDAR really measure in upland ecosystems? Ecohydrology: n/a-n/a. DOI: 10.1002/eco.1527.

Price JC. 1980. The potential of remotely sensed thermal infrared data to infer surface soil moisture and evaporation. Water Resour. Res., **16**: 787-795. DOI: 10.1029/WR016i004p00787.

Quattrochi DA, Luvall JC. 1999. Thermal infrared remote sensing for analysis of landscape ecological processes: methods and applications. Landscape Ecology, **14**: 577-598. DOI: 10.1023/a:1008168910634.

Reed MS, Bonn A, Slee W, Beharry-Borg N, Birch J, Brown I, Burt TP, Chapman D, Chapman PJ, Clay GD, Cornell SJ, Fraser EDG, Glass JH, Holden J, Hodgson JA, Hubacek K, Irvine B, Jin N, Kirkby MJ, Kunin WE, Moore O, Moseley D, Prell C, Price MF, Quinn CH, Redpath S, Reid C, Stagl S, Stringer LC, Termansen M, Thorp S, Towers W, Worrall F. 2009. The future of the uplands. Land Use Policy, **26, Supplement 1**: S204-S216.

Schultz GA, Engman ET. 2011. Remote Sensing in Hydrology and Water Management. Springer Berlin Heidelberg.

Tallis JH. 1998. The southern Pennine experience: an overview of blanket mire degradation. In: Blanket Mire Degradation, Tallis JH, Meade R, Hulme PD (eds.) British Ecological Society, pp: 7–15.

Torgersen CE, Faux RN, McIntosh BA, Poage NJ, Norton DJ. 2001. Airborne thermal remote sensing for water temperature assessment in rivers and streams. Remote Sensing of Environment, **76**: 386-398.

Vierling KT, Vierling LA, Gould WA, Martinuzzi S, Clawges RM. 2008. Lidar: shedding new light on habitat characterization and modeling. Frontiers in Ecology and the Environment, **6**: 90-98. DOI: 10.1890/070001.

Wilson L, Wilson J, Holden J, Johnstone I, Armstrong A, Morris M. 2010. Recovery of water tables in Welsh blanket bog after drain blocking: Discharge rates, time scales and the influence of local conditions. Journal of Hydrology, **391**: 377-386.

Worrall F, Armstrong A, Holden J. 2007. Short-term impact of peat drain-blocking on water colour, dissolved organic carbon concentration, and water table depth. Journal of Hydrology, **337**: 315-325.

568

569 **Table 1: Nominal four point scale for recording near surface water conditions at the catchment.**

Value Criteria	Field Wetness Scale value
Depth to water table > 0.1m	1
Depth to water table < 0.1m	2
Depth to water table = 0m	3
Surface Water	4

570

571

572

573 **Table 2: Summary statistics, semivariogram model parameters and vegetation classification of each AOI attributed**
574 **to each triplet class shown in figure 2.**

Classes of emissivity (see AOIs in figure 2 and semivariograms in figure 4)		Emmisivity mean (SD)	Semivarance Parameters			Dominant land cover
			Nugget	Partial sill	Range	
Red (High emissivity)	A	-0.39 (0.37)	0.003	0.003	2.14	*Juncus effusus* flush
	B	-0.44 (0.26)	0.001	0.003	1.90	Wet bog
	C	-0.22 (0.37)	0.002	0.004	2.37	Wet *Molinea caerulea*
Yellow (intermediate emissivity)	A	-2.05 (0.15)	0.000	0.001	1.93	Minerotrophic grassland
	B	-2.11 (0.15)	0.003	0.003	1.78	*Molinea caerulea*
	C	-2.15 (0.32)	0.002	0.003	2.43	Dry, with stands of *Molinea caerulea*
Blue (low emissivity)	A	-2.94 (0.16)	0.001	0.001	1.53	Dry, with stands of *Molinea caerulea*
	B	-3.12 (0.13)	0.001	0.001	1.38	Dry, with stands of *Molinea caerulea* and *Juncus effusus*
	C	-2.97 (0.15)	0.001	0.001	1.78	Dry *Molinea caerulea*

575

576
577

Figure 1: a) Location of the Spooners Catchment within the UK and b) Exmoor national park. c) LiDAR derived Spooners Watershed and slope contours. d) Aerial photograph of Spooners catchment stretched over LiDAR DEM.

Figure 2: Location of areas of interest (AOI's) measuring approximately 20 m × 20 m. Selected areas of high (Red, >0.64), intermediate (Yellow, -1.51 to -2.6) and low (Blue, <-2.60) Ɛ pixel values identified from the raw TABI. A, B and C denote each triplicate for each classification.

Figure 3: Raw TABI data overlain onto a LiDAR derived DSM and hillshade model. Red areas denote higher emissivity and blue areas lower emissivity. Features of note are highlighted with arrows and labelled accordingly. White line denotes LiDAR defined catchment watershed.

Figure 4: The spatial association of raw TABI data and mapped anthropogenic drainage networks. Arrows labelled as 1, 2 and 3 relate to points made in the accompanying text.

Figure 5: Ordinary spherical semivariogram models for the detrended LiDAR data AOI subsets shown in figure 2. Each plot groups each AOI triplet which exhibit statistically similar Ɛ values in the TABI dataset. a) High Ɛ values, b) intermediate and c) low Ɛ values. For all semivariogram models the lag size used to create the plot is the same as the spatial resolution of the data (0.5 m).

Figure 6: Surface Roughness Index used to normalize TABI data for land surface and vegetation structure.

Figure 7: Results from field survey of soil surface wetness (December 2013). Points are randomly distributed within the catchment, with a minimum allowable distance of 20m. Larger red dots signify the wettest sampled locations.

Figure 8: Visual comparison of a) normalized TABI data shown in Figure 7 and b) Natural Neighbour (NN) interpolation of wetness values collected at survey points.

Figure 9: Boxplot of normalized TABI values which occur at survey location in each separate wetness category (table 1), N = 100.

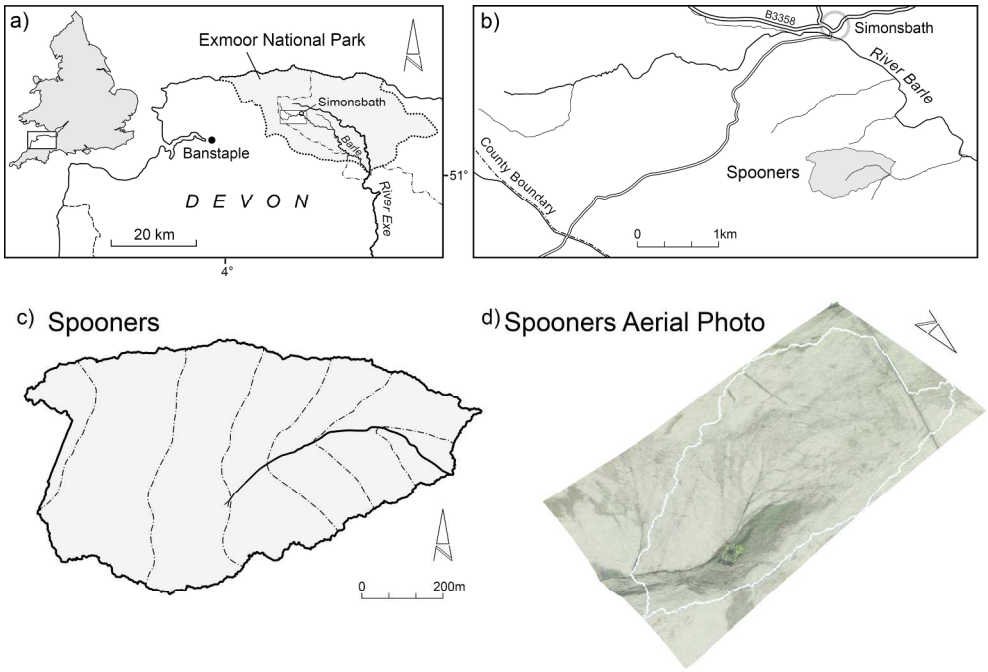

Figure 1: a) Location of the Spooners Catchment within the UK and b) Exmoor national park. c) LiDAR derived Spooners Watershed and slope contours. d) Aerial photograph of Spooners catchment stretched over LiDAR DEM.
112x76mm (600 x 600 DPI)

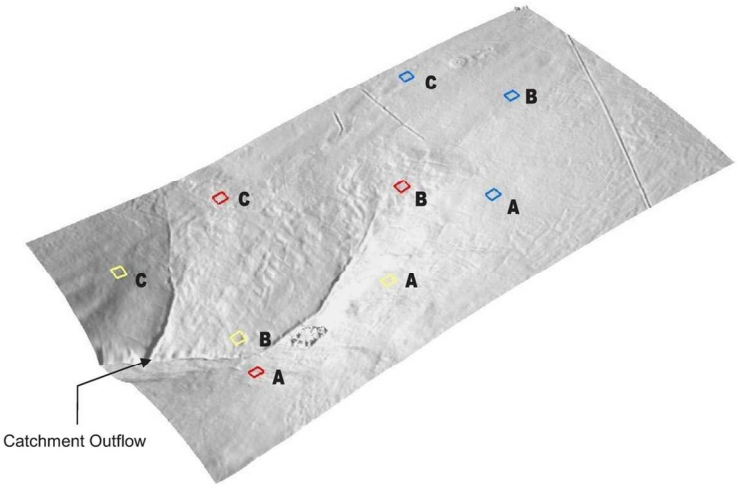

Figure 2: Location of areas of interest (AOI's) measuring approximately 20 m × 20 m. Selected areas of high (Red, >0.64), intermediate (Yellow, -1.51 to -2.6) and low (Blue, <-2.60) Ɛ pixel values identified from the raw TABI. A, B and C denote each triplicate for each classification.
116x64mm (300 x 300 DPI)

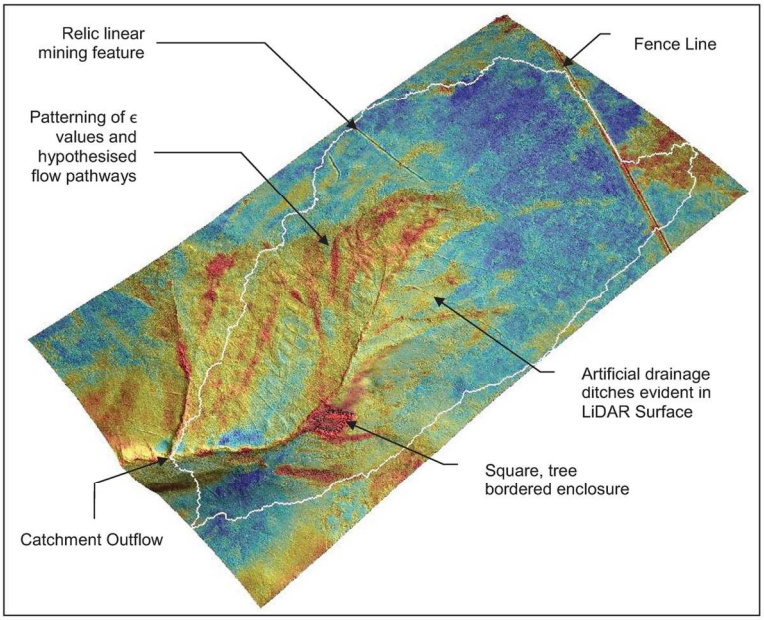

Figure 3: Raw TABI data overlain onto a LiDAR derived DSM and hillshade model. Red areas denote higher emissivity and blue areas lower emissivity. Features of note are highlighted with arrows and labelled accordingly. White line denotes LiDAR defined catchment watershed.
140x94mm (300 x 300 DPI)

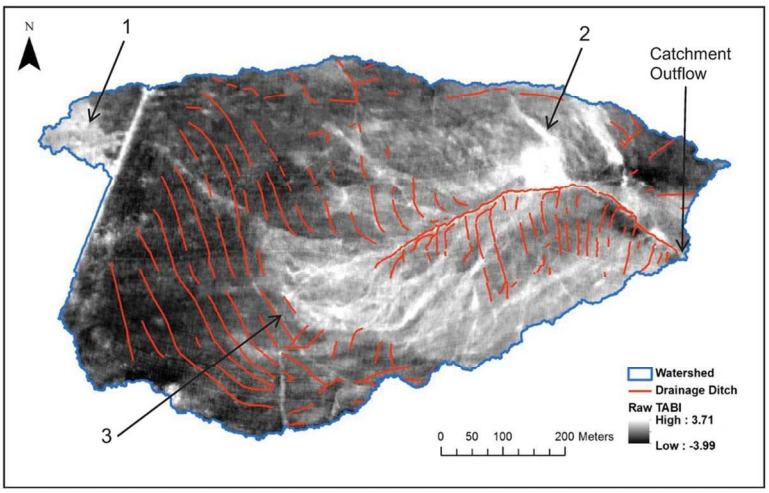

Figure 4: The spatial association of raw TABI data and mapped anthropogenic drainage networks. Arrows labelled as 1, 2 and 3 relate to points made in the accompanying text.
114x62mm (300 x 300 DPI)

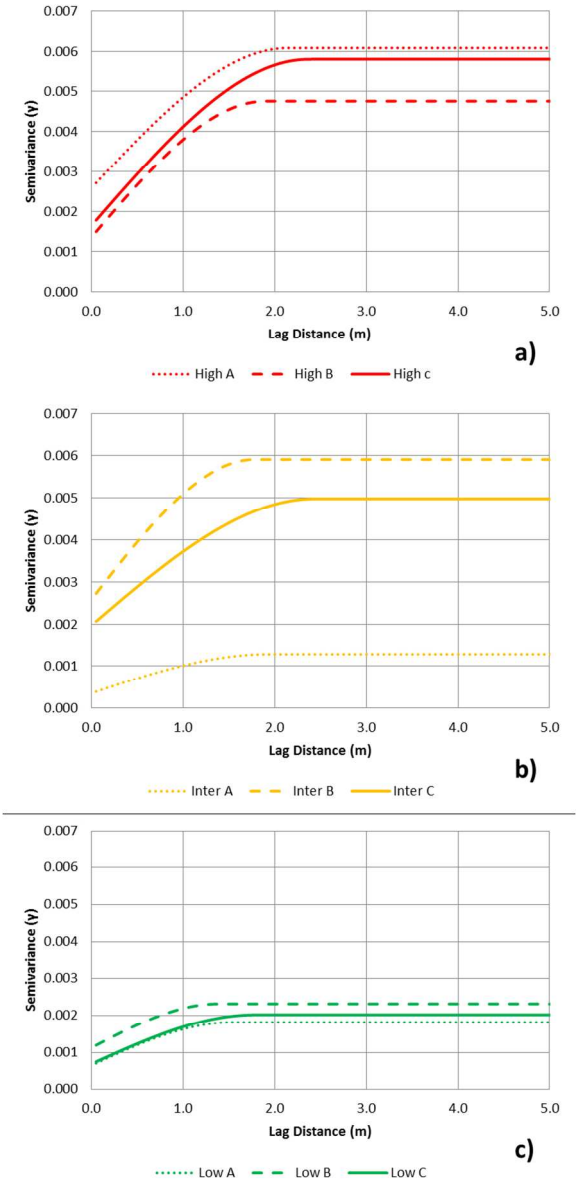

Figure 5: Ordinary spherical semivariogram models for the detrended LiDAR data AOI subsets shown in figure 2. Each plot groups each AOI triplet which exhibit statistically similar Ɛ values in the TABI dataset. a) High Ɛ values, b) intermediate and c) low Ɛ values. For all semivariogram models the lag size used to create the plot is the same as the spatial resolution of the data (0.5 m).
135x283mm (150 x 150 DPI)

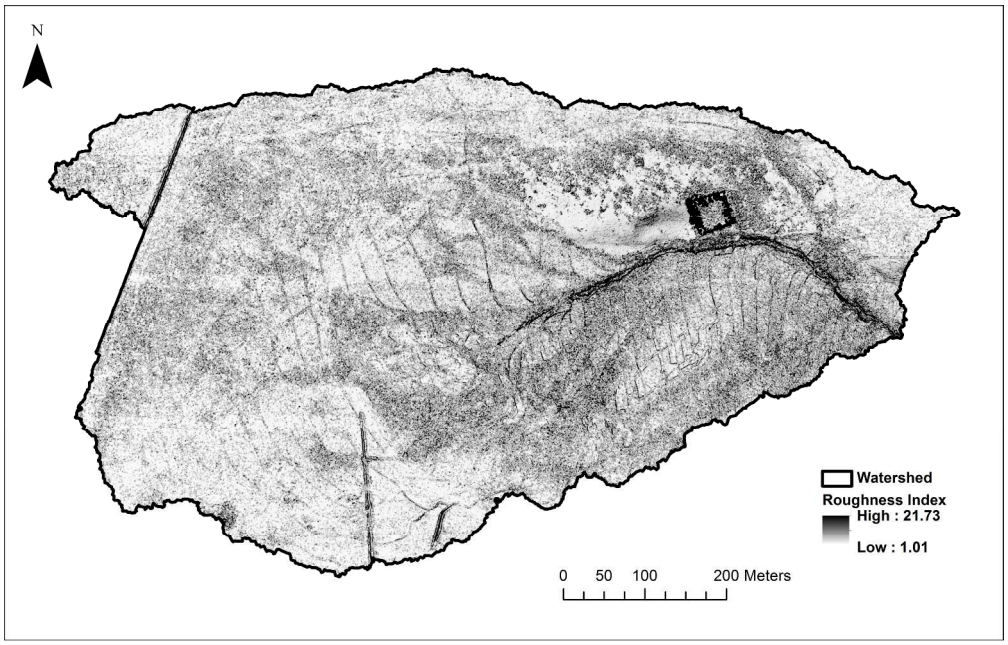

Figure 6: Surface Roughness Index used to normalize TABI data for land surface and vegetation structure.
144x91mm (600 x 600 DPI)

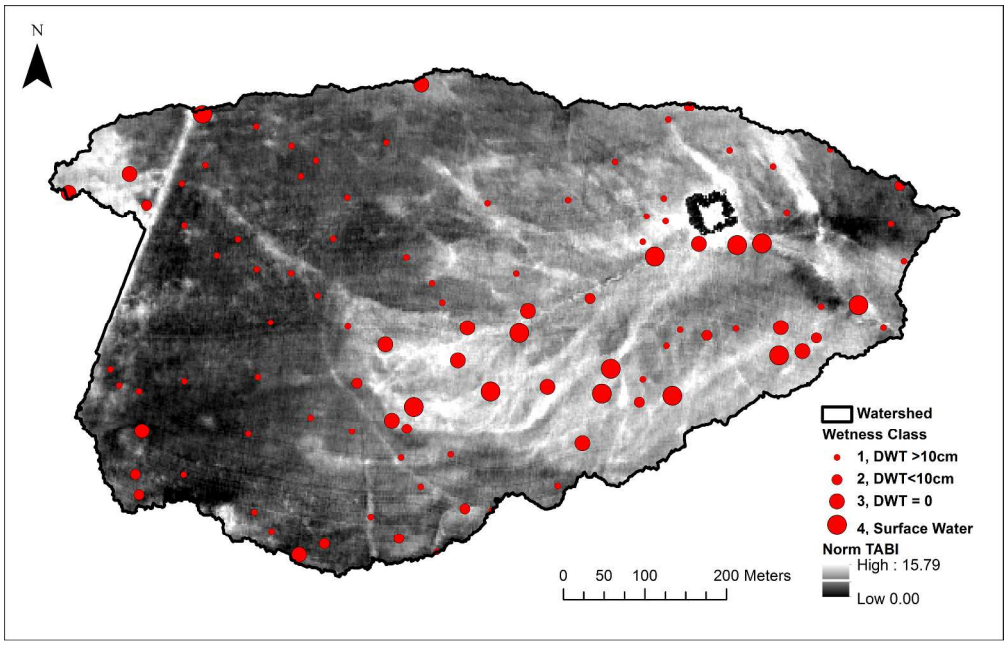

Figure 7: Results from field survey of soil surface wetness (December 2013). Points are randomly distributed within the catchment, with a minimum allowable distance of 20m. larger red dots signify the wettest sampled locations.
144x91mm (600 x 600 DPI)

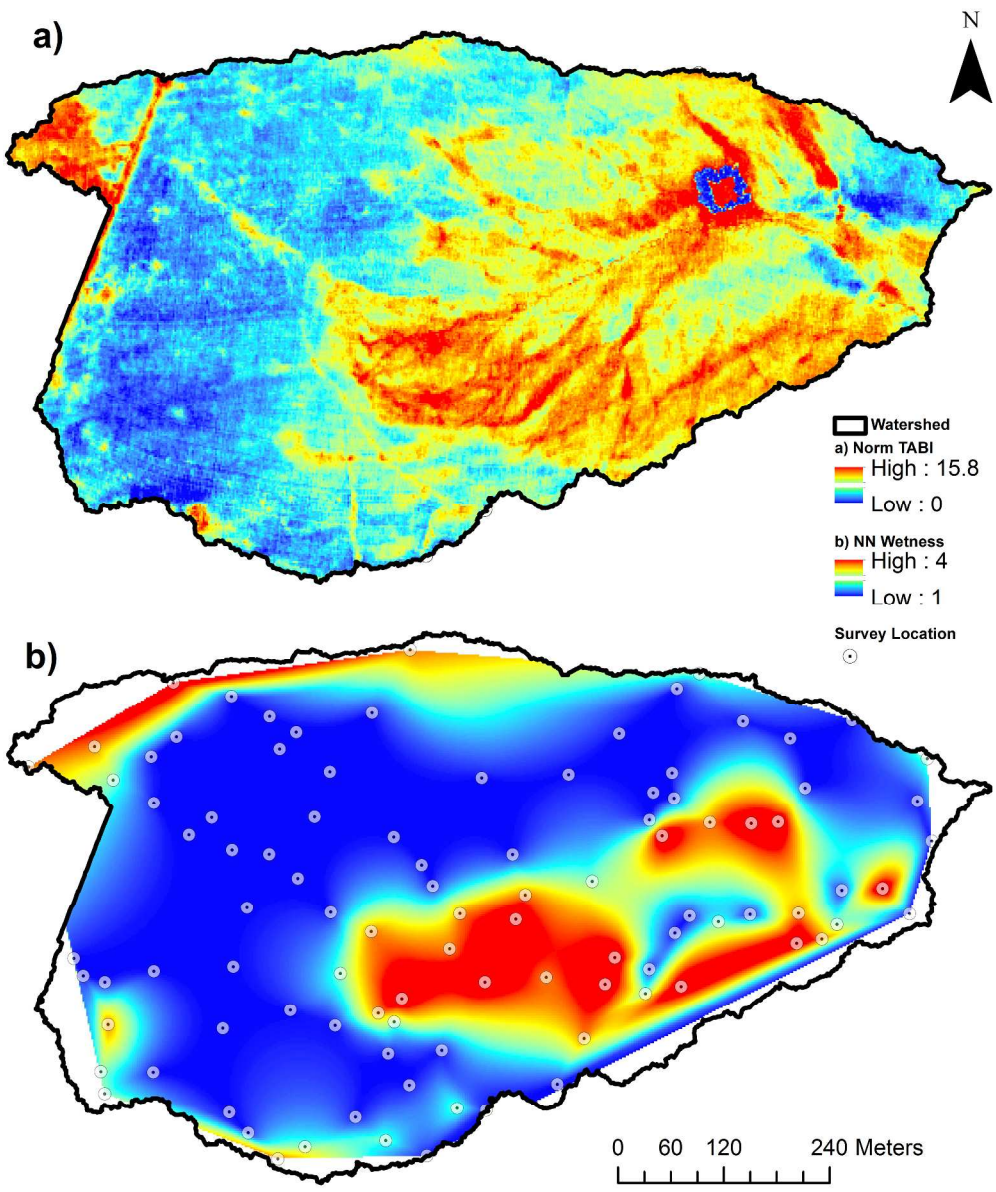

Figure 8: Visual comparison of a) normalized TABI data shown in Figure 7 and b) Natural Neighbour (NN) interpolation of wetness values collected at survey points.
188x228mm (600 x 600 DPI)

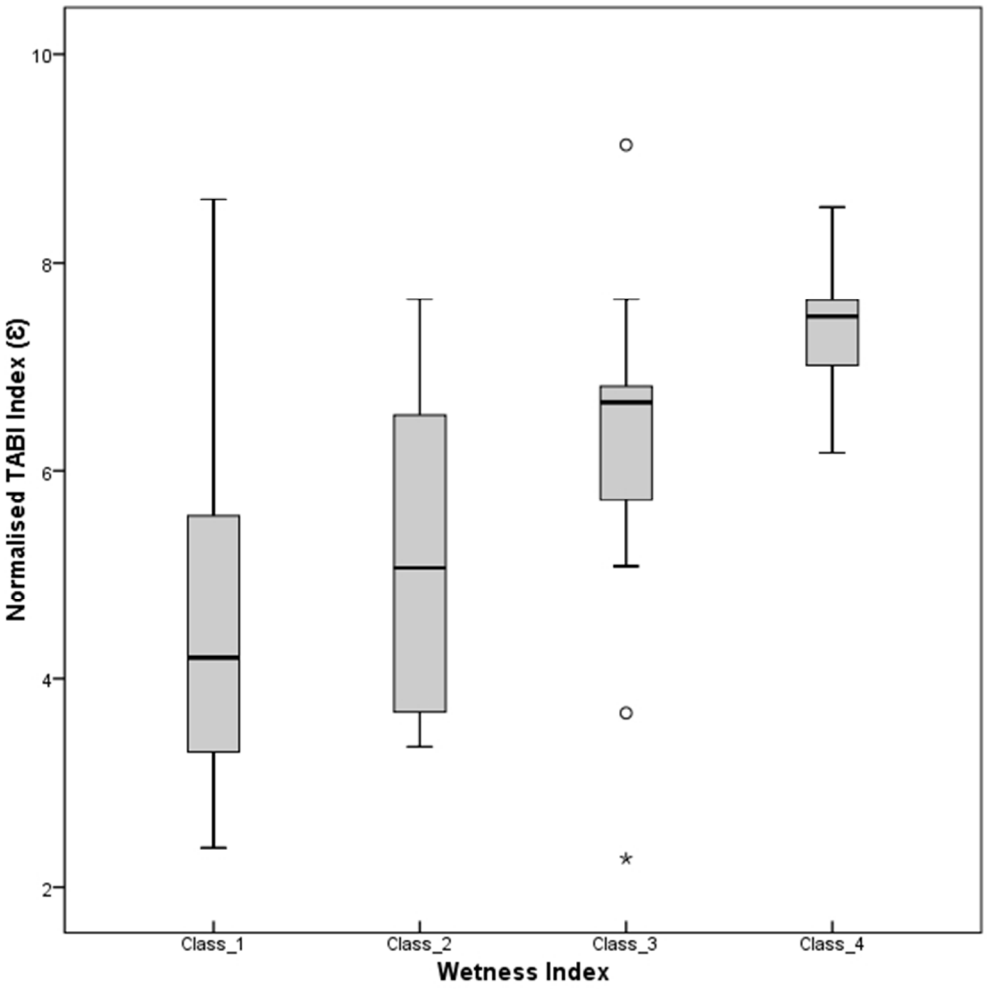

Figure 9: Boxplot of normalized TABI values which occur at survey location in each separate wetness category (table 1), N = 100.
213x213mm (72 x 72 DPI)